university of groningen / faculty of science and engineering / biomedical engineering

Dual Tracer PET Separation: [^{89}Zr]atezolizumab and [^{18}F]FDG

Alesia Vazquez Quiroga

S5046726

Nuclear Medicine and Molecular Imaging Department

Period: 14/04/2025 - 01/07/2025

Bachelor's project

1st Examiner: Harry C. Tsoumpas - Nuclear Medicine and Molecular Imaging Department

2nd Examiner: Marcel Greuter - Radiology Department

Appendix: Declaration on the use of generative AI systems during BME projects

Title of the project:	
Your full name:	
Student number:	

In the project I have used systems based on generative artificial intelligence (AI)[1, 2]
(please check one of the boxes with X).

☐ Yes ☐ No

If you have selected "Yes", complete the rest of the form. If you have selected "No", simply fill in the place, date and signature below.

I have used the following generative AI based systems in the creation of this thesis: [1, 2]
(please list all systems used below)

1.	
2.	
3.	
Other:	

I further declare that I
(please check one of the boxes with X).)

☐ have actively informed myself about the capabilities and limitations of the above-mentioned AI systems to the extent that I can use them responsibly,
☐ have labelled the content taken from the AI systems listed above with my details in the table below,
☐ have verified that the content generated by the above-mentioned AI systems and adopted by me is factually correct,
☐ am aware that, as the author of this work, I am responsible for the information and statements made in it,
☐ am aware that the violation of the disclosure of the use of generative AI in my work is a deception and leads to an evaluation with an insufficient grade.

- Indicate in the table on the next page when the above-mentioned AI systems have been used during your project.
- When you have completed and signed the form, please add it to the beginning of your thesis/report, straight after the standard title page).

[1] This declaration does not apply to the use of basic widely used tools for checking spelling and grammar, translating texts and improving software quality for data analysis and software prototypes.
[2] If you are unsure whether an IT system used is a generative AI system and/or whether you need to declare it, declare it.

I have applied the above-mentioned AI systems as indicated below.

Areas of contribution	Number AI system(s) used	Description of the manner of use and compliance with good scientific practice, if necessary separately by chapter of the work
Development and conception of the research project		
Collection and evaluation of literature sources		
Elaboration, collection and/or procurement of data		
Processing of data		
Selection of methodology		

Programming		
Analysis/evaluation of the data/sources		
Interpretation of the analysis /evaluation and derivation of conclusions		
Writing of the manuscript: Creation of visualizations		
Writing of the manuscript: Structuring the text		
Writing of the manuscript: Formulation of text		

Writing of the manuscript: Revision of text		

Further contributions / additional information:

Place Date Signature

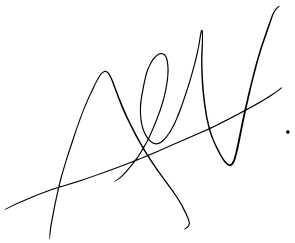

Abstract

Dual-tracer Positron Emission Tomography (PET) enables simultaneous imaging of multiple biological processes, providing improved consistency in physiological and pathological conditions. This study compares two signal separation methods– Extrapolation method (EM) and Background Correction (BC) method for signal separation of 89-Zirconium ([^{89}Zr])-atezolizumab and [18F]2-fluoro-2-deoxy-D-glucose ([^{18}F]FDG). One patient's [^{89}Zr]atezolizumab and dual-tracer scans were used to create noiseless phantoms and simulate ten noise realizations. Tracer separation was performed using both methods and evaluated by various statistical measures using both 10-minute and 30-minute simulated [^{89}Zr]atezolizumab acquisitions. Statistical analyses included normalized root mean square error (NRMSE) for voxel-level comparisons, and standard deviation (SD) versus bias plots and Bland-Altman analyses for ROI-level assessments. Results showed that the 30-minute scan reduced bias in tumor regions for both methods. The EM method outperformed BC in tumor separation, while BC performed better in non-tumor regions, particularly at the voxel level. These findings support the feasibility of dual-tracer separation but highlight the need for larger sample sizes to strengthen statistical power and support clinical translation.

Tables of Contents

1. Introduction

1.1. Dual-Tracer PET

Positron Emission Tomography (PET) is an imaging technique that reveals the metabolic and biochemical function of different organs and tissues, typically co-registered with CT for anatomical data (Trotter et al., 2023). It relies on intravenously injected radioactive tracers, which are biological compounds labeled with positron emitting isotopes that have short half lives, to ensure minimal radiation exposure while allowing physiological equilibrium to be achieved (Tai & Piccini, 2004). Traditionally, dual-tracer imaging required separate scans on different days, increasing patient burden and reducing efficiency. Today, same-day dual tracer PET scans offer a more efficient alternative by minimizing unnecessary waiting time and reducing redundancy (Alberts et al., 2023; Calderón et al., 2025).

Clinically, dual-tracer PET has been used to improve early diagnosis and treatment planning. For example, in neurodegenerative disorders such as Parkinson's disease, both glucose metabolism and dopamine receptor availability provide key diagnostic information. In hepatocellular carcinoma, combining [^{18}F]FDG and ^{11}C-acetate improved lesion detection and led to upstaging in 14.3% of patients (Chiu et al., 2024). Administering both tracers on the same day ensures that the patient 's physiological and pathological state remains consistent, allowing for more accurate comparison and interpretation of complementary biological processes (Lin et al., 2024).

Several protocols have been developed for same-day dual-tracer PET imaging. Liu et al. proposed a method where a low dose of both [^{18}F]FDG followed by [^{68}Ga]Ga-FAPI-04, with static and dynamic scans performed sequentially (Liu et al., 2023). Similarly, Vraka et al. used two fast tracers, performing continuous dynamic scans with [^{11}C]harmine and [^{11}C]DASB to study dynamic brain imaging (Vraka et al., 2022). Meanwhile, technical papers such as Ding et al. have explored kinetic modeling and machine learning to simulate tracer separation using dynamic data from tracers like [^{18}F]FDG and [^{68}Ga]DOTATATE (Ding et al., 2022).

Despite its promise, dual-tracer PET imaging presents challenges. Overlapping tracer kinetics can introduce ambiguity, and signal separation often fails to replicate single-tracer results, leading to potential loss of quantitative accuracy. For example, Kadrmas et al. explain how tracers with similar kinetics, such as 3'-deoxy-3'-18F-fluorothymidine ([^{18}F]FLT) and [^{18}F]FDG, are challenging to separate (Kadrmas et al., 2013). Therefore, using one fast-acting and one slow-acting tracer is ideal for minimizing kinetic overlap and improving separation reliability (Kadrmas & Hoffman, 2013).

This study investigates signal separation of [^{89}Zr]atezolizumab and [^{18}F]FDG using two methods: the extrapolation technique and a background correction method. These tracers form an ideal fast–slow pair, enabling simultaneous imaging of metabolic irregularities and immune checkpoint expression. Using these two tracers allows for simultaneous imaging of irregular metabolism and inhibiting PD-L1, this method aims to improve patient treatment plans and predict therapy response (Bensch et al., 2018). An ideal timeline can be seen in *Figure 1*.

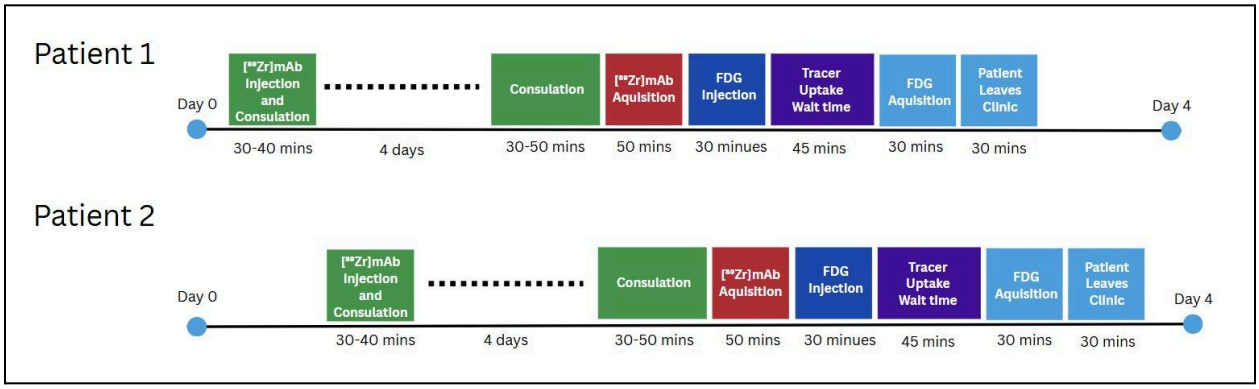

Figure 1. Ideal clinical timeline for same day dual tracer PET signal separation for [^{89}Zr]atezolizumab and [^{18}F]FDG.

1.2. [^{18}F]FDG

[^{18}F]FDG is a glucoses analog in which Fluorine-18 replaced the hydroxyl group at the second position (2-C position) of the glucose molecule. [^{18}F]FDG typically accumulates in tissues with high glucose demand, such as in inflammatory cells and tumors. [^{18}F]FDG is FDA approved in monitoring and evaluating the stage of cancers such as colorectal carcinoma and head and neck cancer in addition to other applications. Prior to injection, glucose levels must be monitored in order to ensure optimal results, this varies per organ of interest (Ashraf & Goyal, 2025). Given its half-life of 109.7 minutes, imaging is required to be done less than three hours after injection (Boellaard et al., 2015).

The typical biodistribution of [^{18}F]FDG is usually follows the pattern outlined below. Uptake is typically observed in the brain, bladder, and liver, in decreasing order (Alfuraih et al., 2021). Additional uptake is seen in the rest of the body due to the abundance of glucose transporters in the body, although the intensity varies by tissue type.

1.3. [^{89}Zr]-atezolizumab

ImmunoPET is a technique which brings together target specificity and sensitivity of monoclonal antibodies (mAbs) and PET radiotracers. This technique enhances the understanding of both tumor heterogeneity, clinical disease management, detecting distant metastases, and unknown lymph nodes. As a result, ImmunoPET can help in early staging, facilitate image guided surgery, and help in characterizing tumor specific antigen expression (Wei et al., 2020).

Atezolizumab is a monoclonal antibody which inhibits PD-L1 and aids in predicting patient therapy response (Bensch et al., 2018). When labeled with [^{89}Zr], the resulting radiotracer has a half-life of 3.3 days, requiring a 4-7 day interval in between tracer injection and imaging to achieve ideal tumor-to-background contrast (Linders et al., 2023). Low uptake of [^{89}Zr]-atezolizumab is observed in the healthy brain, subcutaneous tissue, compact bone, and lungs.

Over time, signal increases in the bone marrow, kidneys, liver, and intestines without the impact of free [^{89}Zr]. In particular, healthy spleen shows a high and variable uptake even in the absence of disease (Bensch et al., 2018).

2. Materials and Methods

2.1. Data Acquisition

Using a mono-tracer [^{89}Zr]-atezolizumab patient scan, dual-tracer [^{89}Zr]-atezolizumab and [^{18}F]FDG scan, and patient activity concentration map, a noiseless phantom was generated to conduct both signal separation methods. The simulation procedure followed the same protocol as the original patient data. Starting with a 30 minute static scan of [^{89}Zr]-atezolizumab 7 days after injection (34.53 MBq) and a dual-tracer scan 66 minutes after 170 MBq [^{18}F]FDG injection.

2.2. Noiseless Phantom Generation Script

Noiseless phantoms for mono tracer [^{89}Zr]-atezolizumab, [^{18}F]FDG, and dual-tracer images were generated based on patient masks using Total Segmentator (*TotalSegmentator: Robust Segmentation of 104 Anatomic Structures in CT Images | Radiology: Artificial Intelligence*, n.d.). These masks were co-registered with the PET data for anatomical overlap and used to assign the uptake of each respective organ.

Four tumors were added to the spleen, liver, and sacrum in random locations without any overlap on all phantoms. The tumors were placed in organs which usually have a high uptake pattern of [^{89}Zr]-atezolizumab, since [^{18}F]FDG is taken up in more organs by comparison (Bensch et al., 2018). Tumor intensities were defined based on a tumor-to-background ratio, with the maximum intensity set to 20 times the average background (organ) activity. Remaining tumor intensity levels were set at 15×, 10×, and 5× the background to simulate a broad range of tumor types (Bensch et al., 2018). Additionally, a background uptake value was taken from the patient's activity concentration image to accurately simulate the original patient image. The background value was taken from three regions of interest (ROI), the arms and neck, with a value of 0.084 as seen in *Figure 2*.

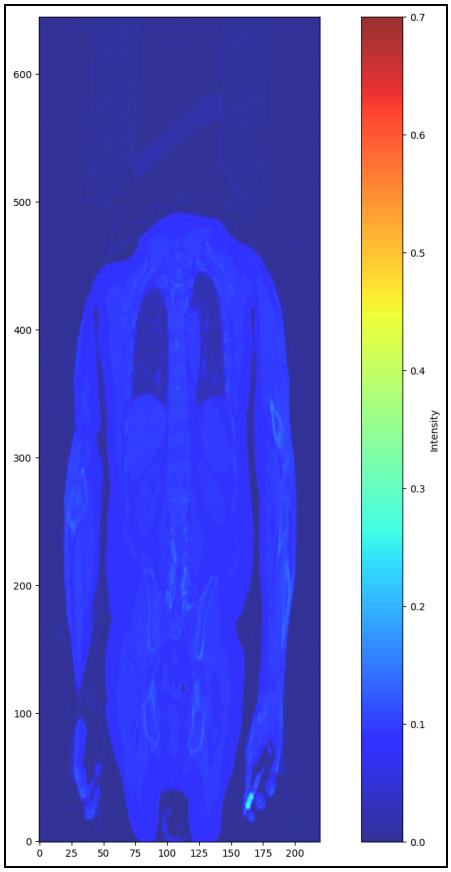

Figure 2. Activity concentration image of patient 1 for background creation on noiseless phantom. The colormap on the right indicates the low activity of the background.

2.3. Noisy Phantom Simulation

All three phantoms were used to simulate full body PET scans based on the Siemens BiographVision Quadra Scanner for ten noise realizations. An example of simulated scans after one noise realization and their respective noiseless phantoms can be seen in Figures 3-5. The drawn ROI on the liver was used for cross validation and can be ignored.

The number of counts simulated for each phantom were based on the counts in the original patient scan. For the [^{89}Zr]-atezolizumab phantom, two simulation times were run by adjusting the number of counts. The number of counts used for each tracer and acquisition time are in Table 1.

Table 1. Counts for Each Scan Protocol

Tracer	Scan Time	Number of counts
[^{89}Zr]-atezolizumab	30 minutes	231341267
[^{89}Zr]-atezolizumab	10 minutes	78694206
[^{18}F]FDG	10 minutes	1182791993
[^{89}Zr]-atezolizumab and [^{18}F]FDG	10 minutes	1182791993

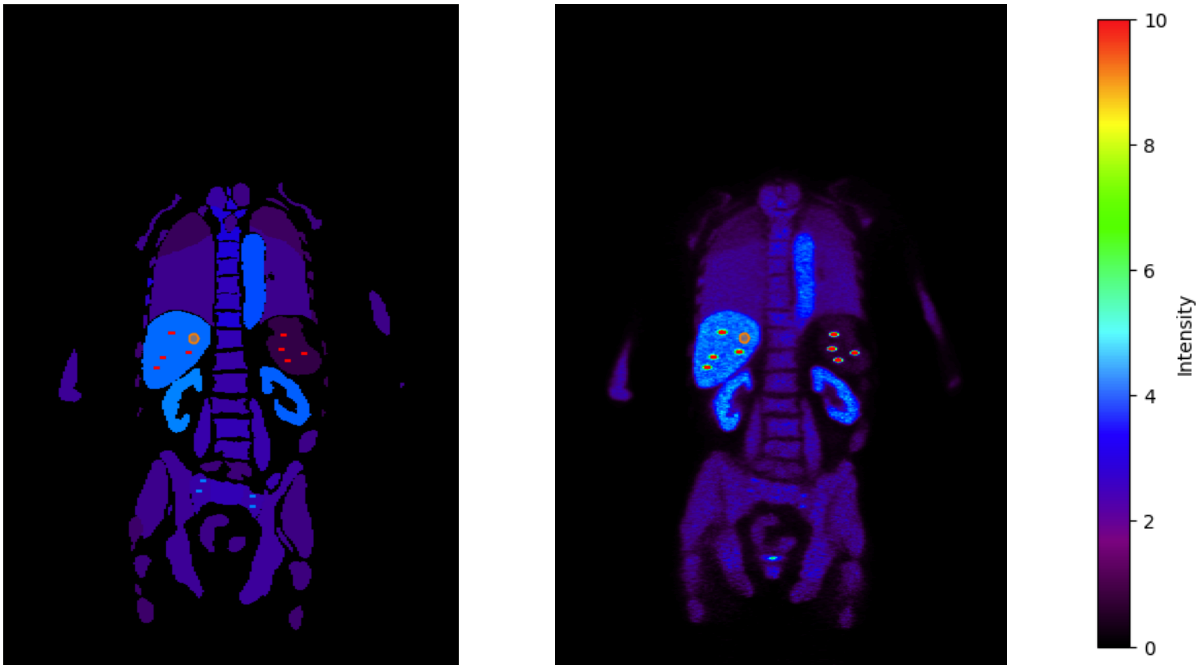

(a) (b)

Figure 3. (a) Noiseless [^{18}F]FDG phantom. (b) Noisy [^{18}F]FDG image scan simulation.

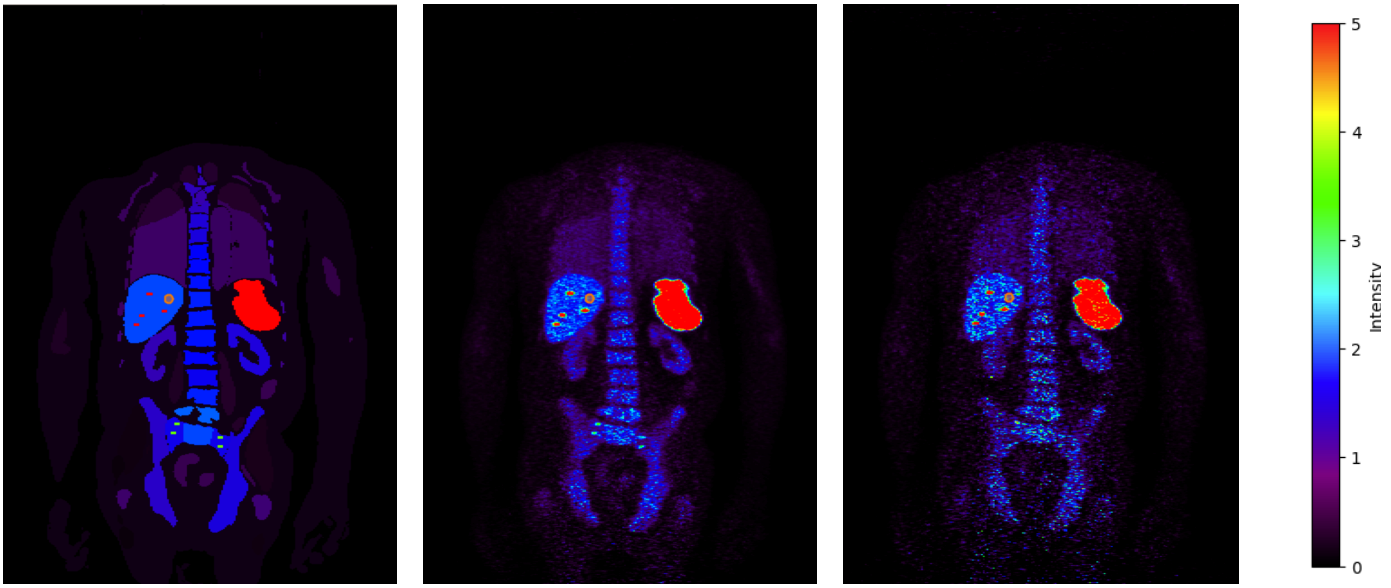

(a) (b) (c)

Figure 4. (a) Noiseless [^{89}Zr]-atezolizumab phantom. (b) Noisy [^{89}Zr]-atezolizumab scan after 30 minute acquisition simulation. (c) Noisy [^{89}Zr]-atezolizumab scan after 10 minute acquisition simulation.

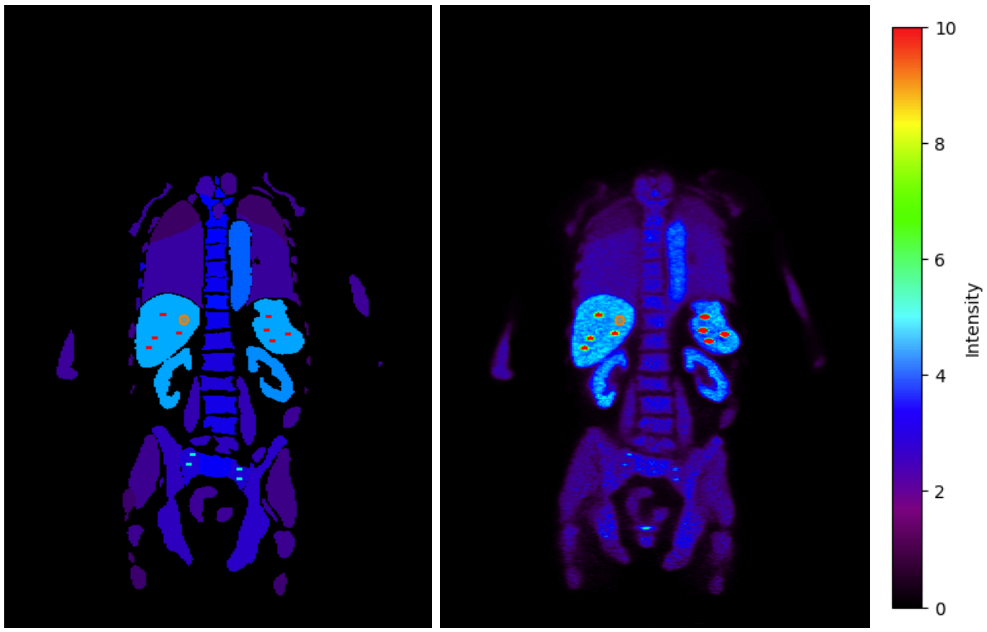

(a) (b)

Figure 5. (a) Noiseless dual-tracer phantom. (b) Noisy dual-tracer scan after simulation.

2.4. Signal Separation Methods

Two different methods were used to compare signal separation of [^{89}Zr]-atezolizumab and [^{18}F]FDG using a monotracer [^{89}Zr]-atezolizumab and dual-tracer [^{89}Zr]-atezolizumab and [^{18}F]FDG image.

2.4.1. Background Correction

Ordered Subsets Expectation Maximization (OSEM) reconstruction is an iterative reconstruction method in PET imaging. OSEM back projects part of the data to speed up reconstruction, where each image is used as an input when acting on the next subset. This method allows for faster reconstruction with increasing subsets and reduces the loss of small artifacts (Defrise et al., 2005). Background correction is a method based on the slow decay and kinetics of [^{89}Zr]-atezolizumab as it can be assumed to be constant. In order to correct for the signal contribution of [^{89}Zr]-atezolizumab, it is modeled as a background term in addition to an additive term in standard OSEM reconstruction using 5 subsets for 20 iterations (Tsoumpas & Thielemans, 2009).

$$\lambda_j^{(n+1)} = \frac{\lambda_j^{(n)}}{\sum_{i \in J_j} H_{ij}' M_i} \sum_{i \in J_j} H_{ij}' \frac{y_i M_i}{H_{ik}' \lambda_k^{(n)} + A_i + T_i} \quad \text{[E.1]}$$

2.4.2. Extrapolation Method

The extrapolation Method (EM) is based on the original approach from Koeppe et al. in 2004 which assumes that the injection protocol brings the reference region of the first tracer to equilibrium before the second tracer is injected (Joshi et al., 2008). In this study, EM was used to to isolate [^{89}Zr]-atezolizumab, by extrapolating the [^{89}Zr]-atezolizumab signal and subtracting it from the dual tracer generated phantom. Due to the slow tracer kinetics of [^{89}Zr]-atezolizumab, it can be assumed that the [^{89}Zr]-atezolizumab is constant from the time of the mono-tracer scan to the dual tracer scan.

$$C_{PET}^{[^{18}F]FDG} = \frac{1}{T_2 - T_1} \int_{T_1}^{T_2} (C_T^{Dual}(u) - C_T^{[^{89}Zr]mAb}(u)) du \quad \text{[E. 2]}$$

2.5. Data Analysis

Before conducting the following data analysis, visual checks were done to ensure that tumor and organ masks overlapped correctly across all acquired images. Different methods were used to analyze the acquired data in accordance with the number of data points collected.

2.5.1. Bland-Altman Plot

To visualize the difference between the EM and BC methods, two Bland-Altman plots were created. The percent intensity difference between the outputs of each method and the average of the [^{18}F]FDG simulation output (ground truth) were compared for tumors and organs of interest over the 3D image (Bland & Altman, 1999).

2.5.2. Normalized Root Mean Square Error (NRMSE)

To evaluate the quality of the separated tracer images, the separation method for mono-tracer [^{18}F]FDG scan was evaluated over R = 10 noise realizations using the voxel-level NRMSE (Pan et al., 2025). NRMSE was calculated by

$$NRMSE = \sqrt{Bias^2 + SD^2} \quad \text{[E. 3]}$$

With bias and standard deviation (SD) defined as

$$Bias = \sqrt{\frac{\sum_{j\in\Omega}(\bar{x}_j - x_j^{Ref})^2}{\sum_{j\in\Omega}(x_j^{Ref})^2}} \times 100\% \;, SD = \sqrt{\frac{1}{R}\frac{\sum_{r=1}^{R}\sum_{j\in\Omega}(\bar{x}_j - x_j^{r})^2}{\sum_{j\in\Omega}(x_j^{Ref})^2}} \times 100\% \quad \text{[E. 4]}$$

Additionally, the ROI-level bias and SD were also calculated for the tumor regions and chosen organs with bias and SD deviation defined as

$$ROI - Bias = \frac{1}{c^{Ref}}|\bar{c} - c^{Ref}| \times 100\% \,, ROI - SD = \frac{1}{c^{Ref}}\sqrt{\frac{1}{R}\sum_{r=1}^{R}|\bar{c} - c^{r}|^2} \times 100\% \quad \text{[E. 5]}$$

Using the values of bias and SD, scatter plots were created to visualize the impact of each metric individually.

2.5.3. Statistical Analysis

2.5.3.1. Two Way Analysis of Variance Test

A two way analysis of variance (ANOVA) was computed on an ROI-level to compare the following metrics:

- 10 minute vs. 30 min [^{89}Zr]-atezolizumab acquisition for EM
- 10 minute vs. 30 min [^{89}Zr]-atezolizumab acquisition for BC

A two way ANOVA test allowed for comparison of signal separation using a 10 minute vs. 30 min [^{89}Zr]-atezolizumab for both methods.

3. Results

3.1. Ground Truth and Separated Images

Figure 6 presents the average ground truth image and the corresponding separated [^{18}F]FDG signal across all 10 noise realizations for each separation method. As shown in panels a, b, and c, the uptake patterns in the spleen, sacrum, and liver remain consistent across separation methods when compared to the ground truth. Additionally, the average ground truth image for [^{89}Zr]-atezolizumab is shown in panel d.

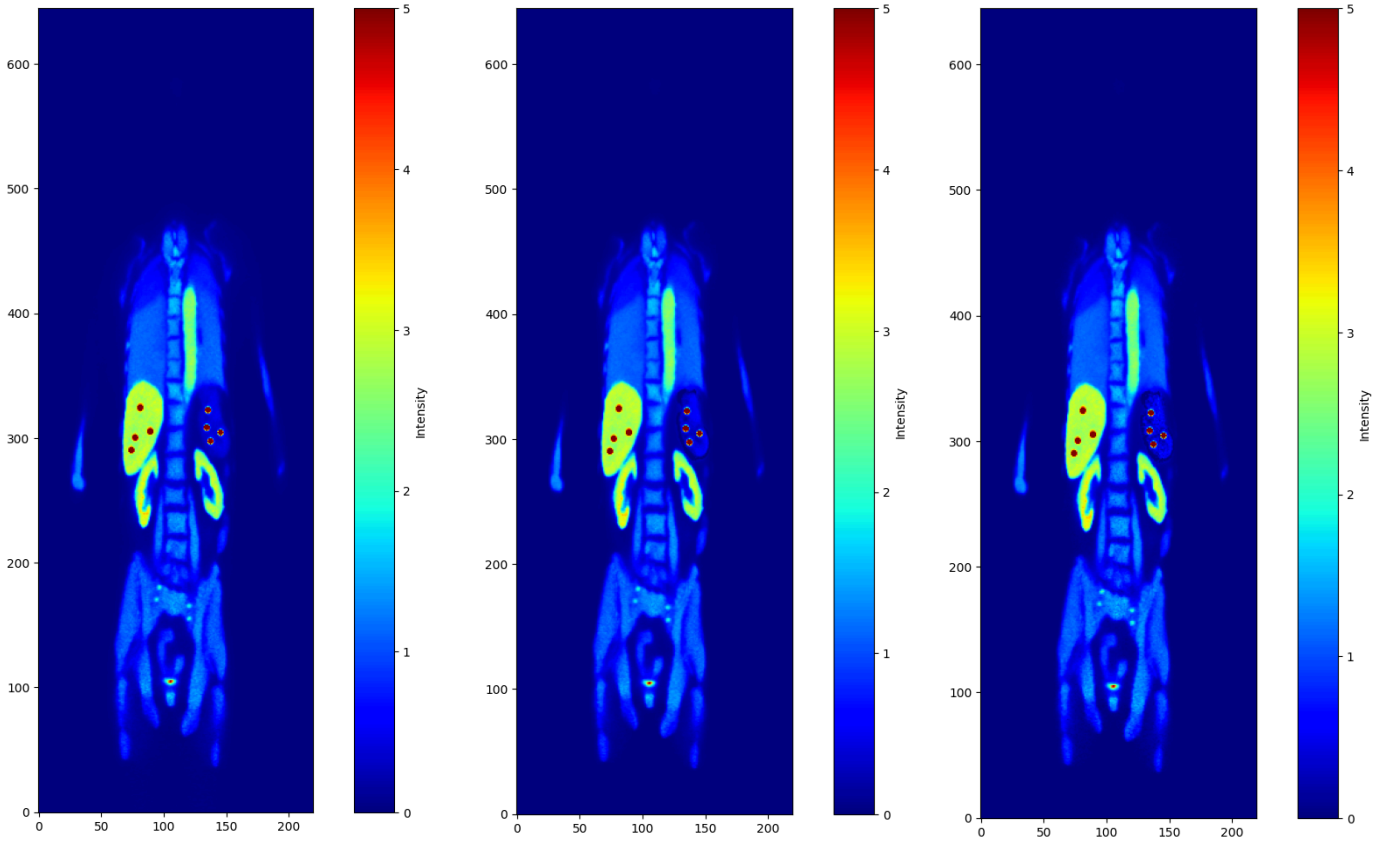

(a) (b) (c)

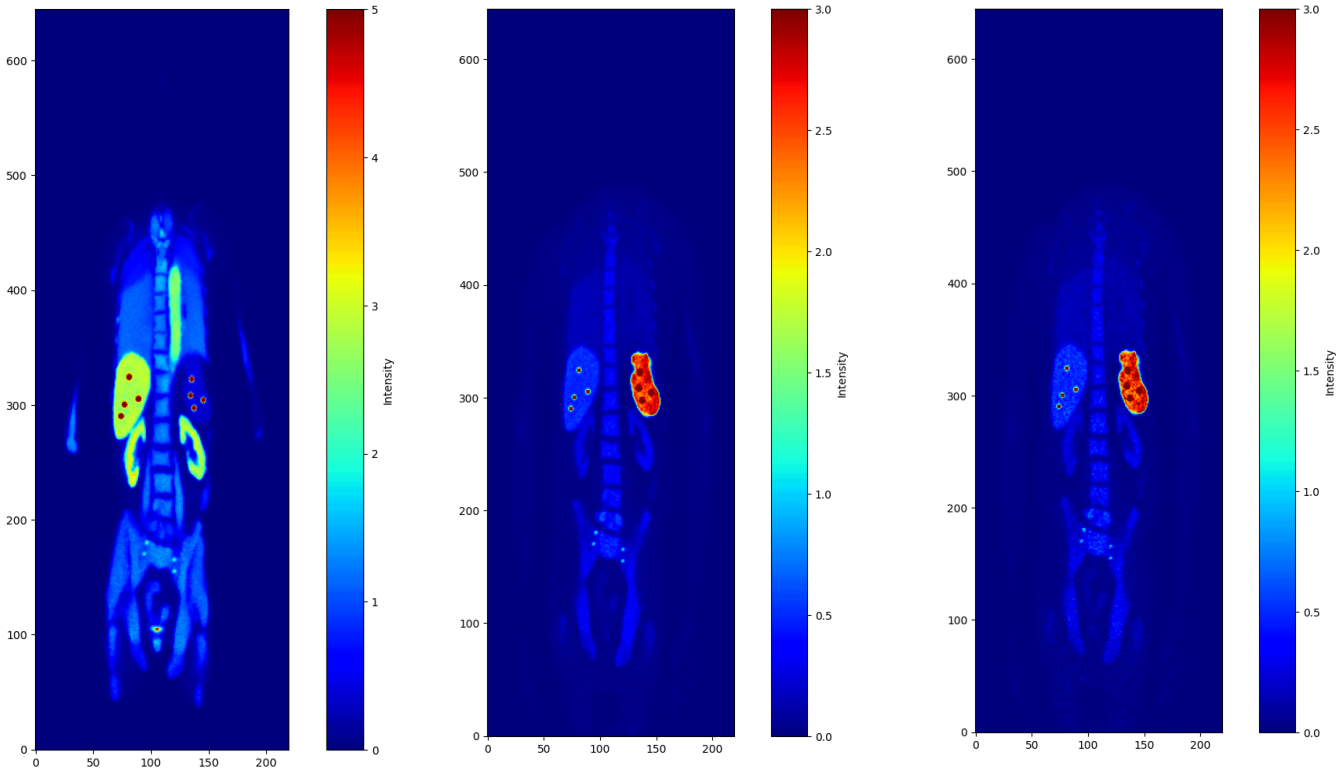

(d) (e) (f)

Figure 6. (a) [^{18}F]FDG ground truth. (b) [^{18}F]FDG separated signal using EM with 30 minute [^{89}Zr]-atezolizumab. (c) [^{18}F]FDG separated signal using EM with 10 minute [^{89}Zr]-atezolizumab. (d) [^{18}F]FDG separated signal using BC with 30 minute [^{89}Zr]-atezolizumab. (e) [^{18}F]FDG separated signal using BC with 10 minute [^{89}Zr]-atezolizumab. (f) 30 minute [^{89}Zr]-atezolizumab acquisition ground truth. (g) 10 minute [^{89}Zr]-atezolizumab acquisition ground truth.

3.2. Separation with 30 minute [^{89}Zr]-atezolizumab Acquisition

To compare the EM and BC methods, a Bland-Altman plot (Figure 7) illustrates the ROI-level differences for all regions. For both methods, the difference fall within the confidence interval of 96%, indicating agreement with the ground truth [^{18}F]FDG scan. The data tables can be found in Appendix 7.1.1 .

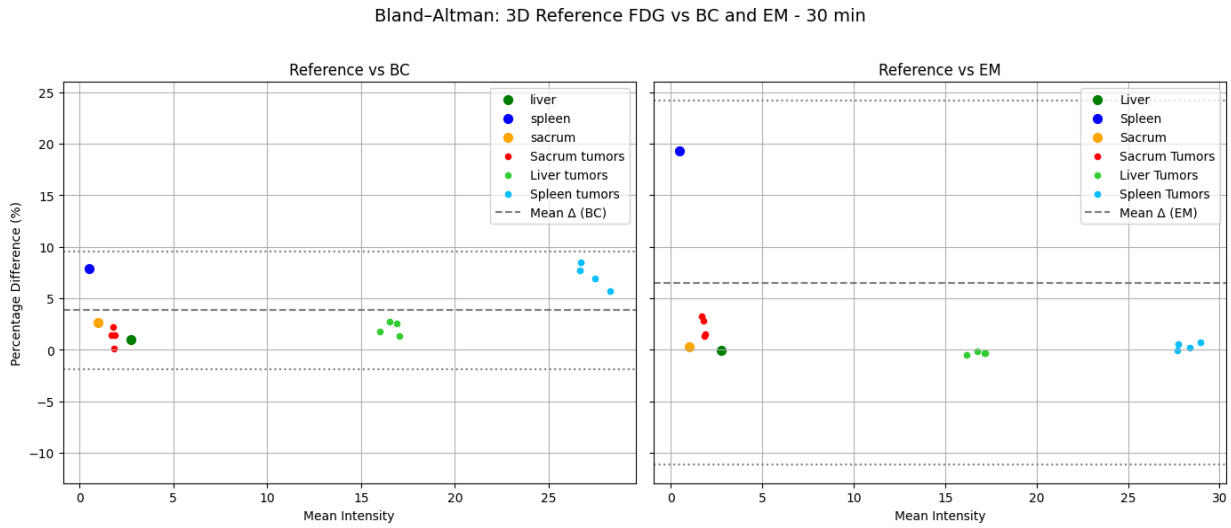

(a) (b)

Figure 7. (a) Bland-Altman plot: Reference [18F]FDG vs. BC method. (b) Bland-Altman plot: Reference [18F]FDG vs. EM method.

Figure 8 illustrates the ROI-level SD versus bias for each organ and its corresponding tumor, comparing the EM and BC methods. The BC method consistently shows lower SD across all regions. In contrast, the EM method yields lower bias for all organs and tumors except for the spleen and sacrum tumors, as seen in Figure 8a. The data corresponding tables can be found in Appendix 7.1.2 .

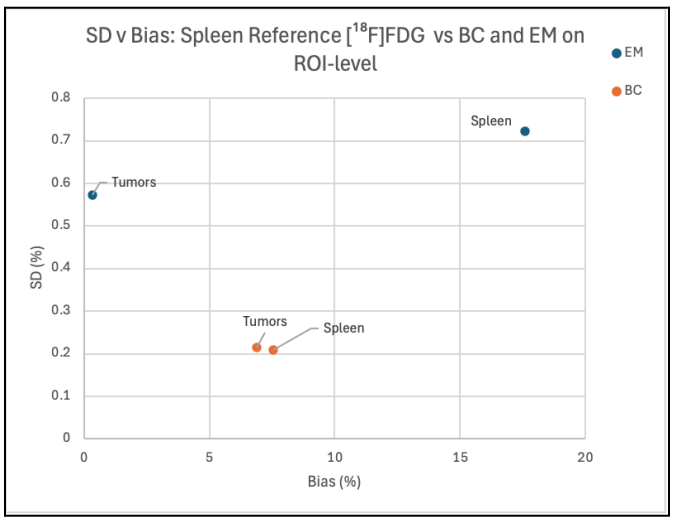

(a)

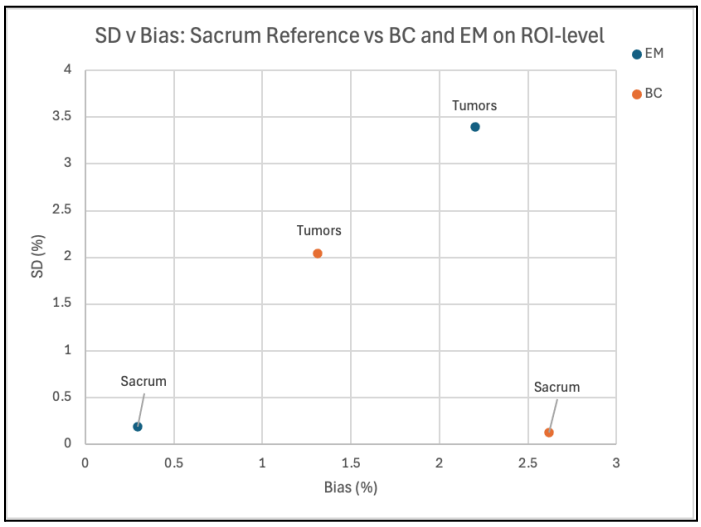

(b)

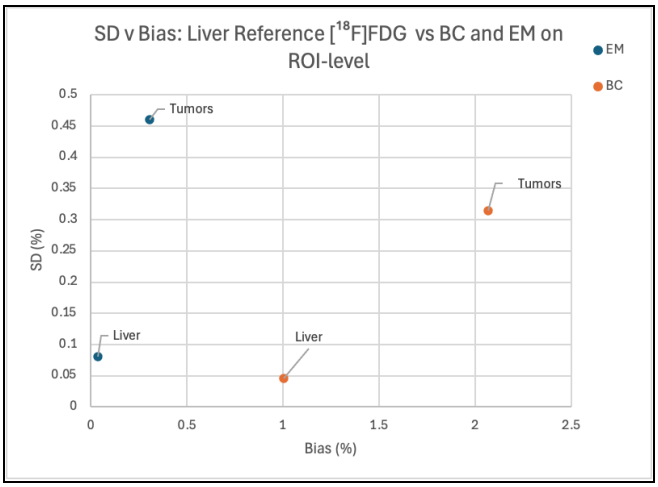

(c)

Figure 8. (a) SD vs. bias for the spleen: BC vs. EM. (b) SD vs. bias for the sacrum: BC vs. EM. (c) SD vs. bias for the liver: BC vs. EM.

On a voxel-level, the EM and BC methods are compared using NRMSE, as shown in Figure 9a. The corresponding SD and bias are presented in Figure 9b. For tumor regions, the EM outperforms BC, whereas BC performed better in organ regions. The lower NRMSE observed for the EM in tumors is primarily due to the reduced bias than SD.

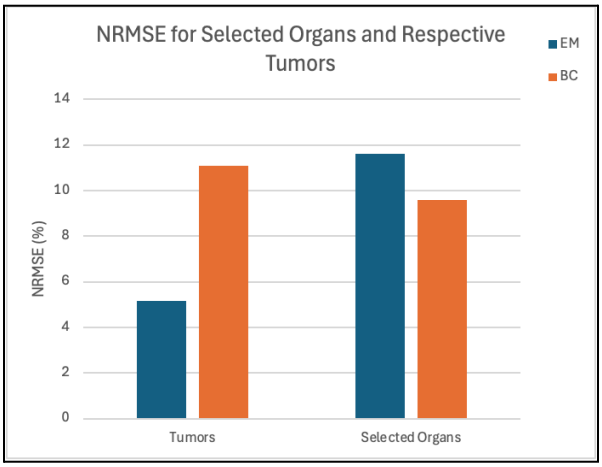

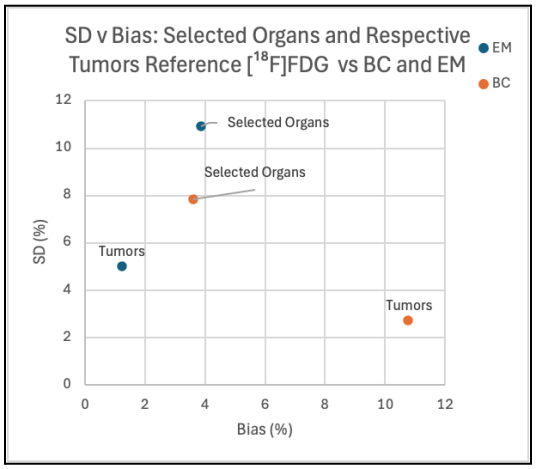

(a) (b)

Figure 9. (a) Voxel-level NRMSE comparison between EM (blue) and BC (green) across selected organs and their corresponding tumors. (b) Decomposition of NRMSE into SD and bias components.

3.3. Separation with 10 minute [^{89}Zr]-atezolizumab Acquisition

To compare the EM and BC methods, a Bland-Altman plot (Figure 10) illustrates the ROI-level differences for all regions. For both methods, the difference fall within the confidence interval of 96%, indicating agreement with the ground truth [^{18}F]FDG scan. The data tables can be found in Appendix 7.2.1 .

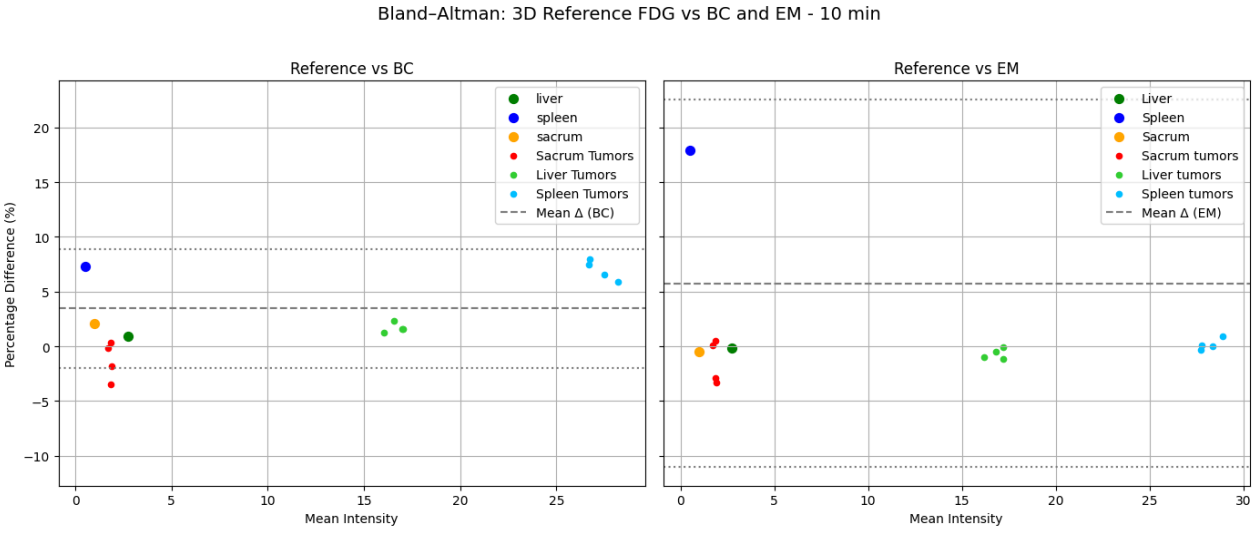

(a) (b)

Figure 10. (a) Bland-Altman plot: Reference [^{18}F]FDG vs. BC method. (b) Bland-Altman plot: Reference [^{18}F]FDG vs. EM method.

Figure 11 illustrates the ROI-level SD versus bias for each organ and its corresponding tumor, comparing the EM and BC methods. The BC method consistently shows lower SD across all regions. In contrast, the EM method yields lower bias for all organs and tumors except for the spleen and sacrum tumors, as seen in Figure 11a. The data corresponding tables can be found in Appendix 7.2.2.

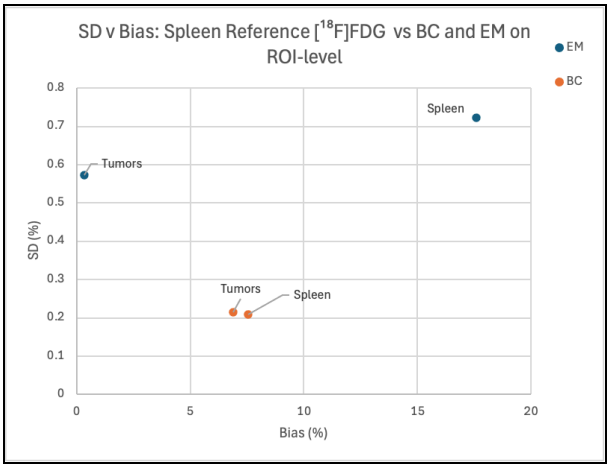

(a)

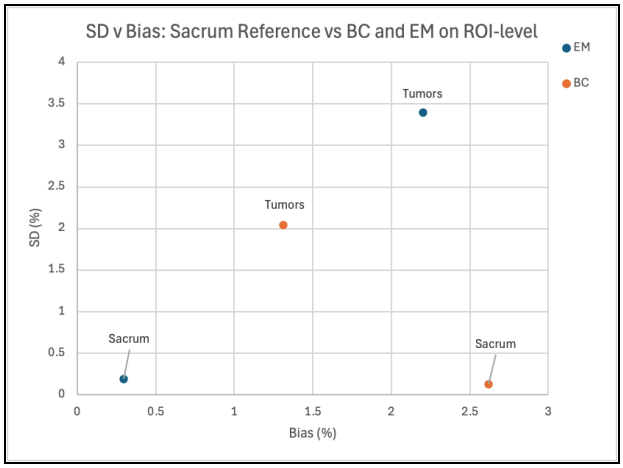

(b)

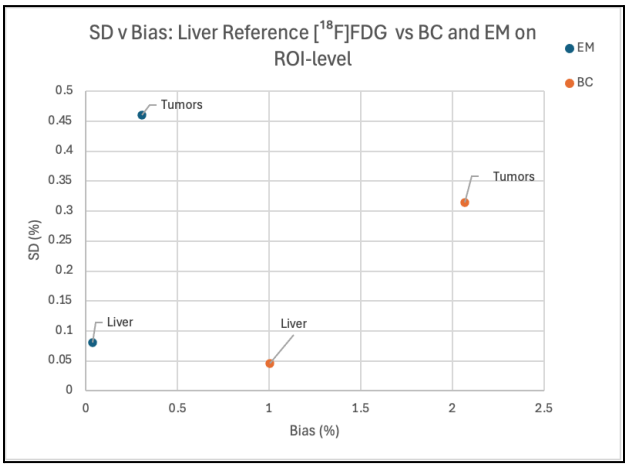

(c)

Figure 11. (a) SD vs. bias for the spleen: BC vs. EM. (b) SD vs. bias for the sacrum: BC vs. EM. (c) SD vs. bias for the liver: BC vs. EM.

On a voxel-level, the EM and BC methods are compared using NRMSE, as shown in Figure 12a. The corresponding SD and bias are presented in Figure 12b. For tumor regions, the EM outperforms BC, whereas BC performed better in organ regions. The lower NRMSE observed for the EM in tumors is primarily due to the reduced bias than SD.

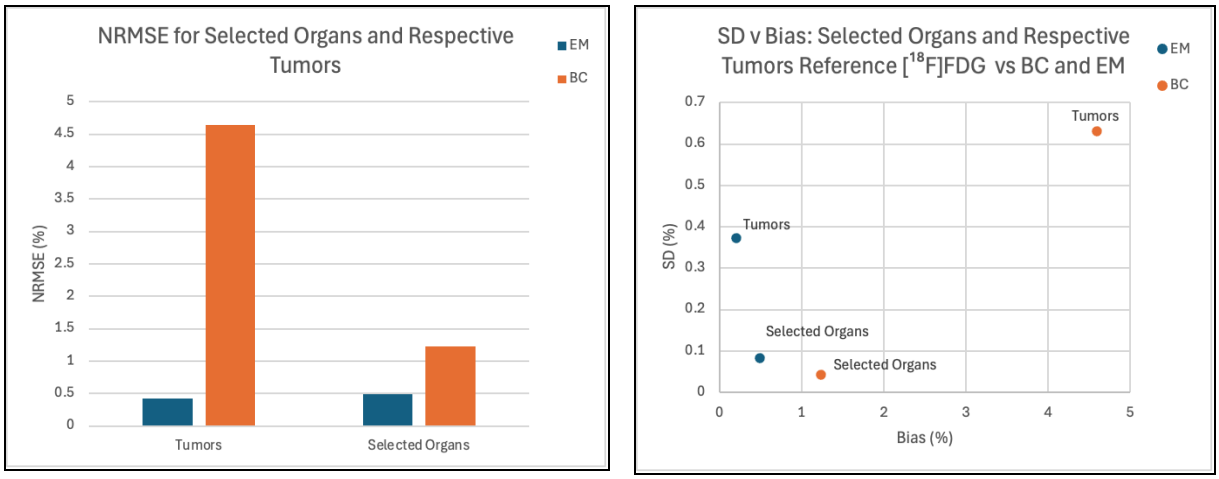

(a) (b)

Figure 12. (a) Voxel-level NRMSE comparison between EM (blue) and BC (green) across selected organs and their corresponding tumors. (b) Decomposition of NRMSE into SD and bias components.

3.4. Separation with 30 minute v. 10 minute [^{89}Zr]-atezolizumab Acquisition

A two-way ANOVA test was conducted to compare the effects of acquisition time (30 minute vs. 10 minute) and separation method (EM vs. BC) on [^{18}F]FDG signal recovery. Statistical significance was found as per the p-values of 0.01500970745. The ANOVA summary table is found in Appendix 7.3.1 .

4. Discussion

This study assessed the performance of the EM and BC methods for dual-tracer PET signal separation, focusing on both tumor and organ regions. While prior research has demonstrated the feasibility of separating tracers using simplified models or in specific anatomical regions (A.D. Joshi et al., 2008), few studies have compared these two methods across varying acquisition times. To address this gap, a combination of ROI- and voxel-based analyses alongside Bland-Altman plots, bias versus SD comparisons, NRMSE, and two-way ANOVA were used to evaluate differences between each separation method and the ground truth [^{18}F]FDG image.

A general observation across all analyses was that voxel-wise metrics exhibited greater variability (higher SD) than ROI-level results, which is consistent with previous findings due to elevated noise at the voxel level (Greve et al., 2014). As a result, ROI-level data were emphasized in key evaluations. Prior literature suggests that non-invasive separation methods typically achieve deviations within 10% of the ground truth (Joshi et al., 2008) serving as a reference point for evaluating both methods' performance.

4.1. Separation with 30 minute [^{89}Zr]-atezolizumab

To evaluate the EM and BC methods using a 30-minute [^{89}Zr]-atezolizumab acquisition, separated [^{18}F]FDG signals across individual tumors and selected organs were compared using multiple statistical tools. The Bland-Altman plot (Figure 7) highlighted method-specific differences from the reference [^{18}F]FDG image at the ROI level. The EM produced a smaller percent difference than BC in the liver and sacrum, whereas the BC method was more accurate in the spleen. This discrepancy in the spleen is likely due to its characteristically low [^{18}F]FDG uptake and high signal from [^{89}Zr]-atezolizumab in the background image—resulting in the EM to overestimate uptake more than BC. These trends are consistent with known challenges in regions with low tracer uptake and high signal interference (Joshi et al., 2008).

Tumor-level performance varied by anatomical location. The EM outperformed BC in tumors located within the liver and spleen, while BC showed lower bias in tumors situated in the sacrum. Since tumor intensity was altered according to respective organ uptake, sacral tumors have intermediate signal levels, resulting in smaller differential contrast between [^{89}Zr]-atezolizumab and [^{18}F]FDG, making BC more favorable in such contexts (Kadrmas & Hoffman, 2013). Importantly, despite these differences, all regions remained within the 95% confidence interval, suggesting both methods maintained acceptable agreement with the ground truth. However, the EM method's 17.58% bias in the spleen may exceed clinically acceptable thresholds in certain applications.

Further bias and variability were explored through SD versus bias plots (ROI-level) and NRMSE at the voxel level. In the spleen, the organ with the lowest [^{18}F]FDG uptake, the EM exhibited greater bias and higher SD than BC, supporting the earlier conclusion of EM overestimation. For

tumors in the spleen, the trend was reversed, the BC underestimated tumor uptake compared to EM (Figures 8a, 9a, and 9b).

In the sacrum, BC was favored for tumors, while the EM showed better accuracy for the organ. The mean bias difference between methods for sacral tumors was modest at 0.15% (ROI) but more pronounced at 3.25% (voxel), reinforcing the impact of noise at finer spatial resolutions. For the liver, exhibiting the highest [^{18}F]FDG uptake, the EM consistently outperformed BC on both ROI and voxel-levels, aligning with earlier observations from Bland-Altman plots. Nevertheless, the voxel-level bias difference between methods in the liver was minimal (0.09%), suggesting that either method could be feasible in high-uptake regions.

4.2. Separation with 10 minute [^{89}Zr]-atezolizumab

The same analytical approach was applied to evaluate 10-minute [^{89}Zr]-atezolizumab scans. Results from the Bland-Altman plot (Figure 10) were consistent with those from the 30-minute scans. The EM method performed better for tumor regions, while the BC method had an advantage for selected organs at the voxel level.

Further evaluation using bias vs. SD plots and NRMSE provided insight into method-specific behavior. The spleen again showed higher bias and NRMSE for the EM, supporting previous conclusions. In the sacrum, BC was favored at the ROI-level, with a bias difference of 5.53%, (Figure 11b). For the liver, the EM method showed improved performance, particularly at the voxel level (1.33% vs. 0.09% in the 30-minute scan). Overall, ROI-level trends remained consistent across both acquisition durations. Standard deviation did not notably change between acquisition times, suggesting that noise levels had a limited impact on SD vs. bias relationships.

4.3. Separation with 30 minute v 10 minute [^{89}Zr]-atezolizumab

Two-way ANOVA was used to compare the performance of each method using 30-minute vs. 10-minute [^{89}Zr]-atezolizumab scans. For the BC method, significant differences were found between acquisition times and tumor regions, with F-values exceeding the critical threshold (Appendix 7.3.1). This indicates that the 30-minute scan was more effective for signal separation in tumors. The same conclusion was reached for the EM method.

These results suggest that the 30-minute scan provides more reliable signal separation for both EM and BC methods. This is likely due to reduced noise, as visualized in Figures 4b and 4c. Lower total counts in the 10-minute scan contributed to slightly higher bias and variability (Cui et al., 2019).

4.4. Limitations

Several limitations should be considered. Most notably, the study was based on a single patient scan, and although ten noise realizations were used to increase data variability, the overall

sample size remained small. This limited the statistical power of certain analyses and restricted generalizability. Only three organs were analyzed in detail, which limits the translation of the conclusions, specifically for organ-level comparisons.

4.5. Future Outlook and Clinical Implications

Future research should involve more patient data, evaluate a wider range of anatomical regions, and investigate separation with different tracers. Increasing sample size would enhance statistical reliability. In addition, feedback from clinical practitioners would be valuable to assess the practical feasibility of implementing these separation methods in clinical workflows.

4.6. Conclusion

This study assessed the EM and BC methods for separating [^{89}Zr]-atezolizumab and [^{18}F]FDG signals in dual-tracer PET scans. Using several statistical methods—including ANOVA, voxel-wise NRMSE, and SD vs. bias plots—the EM method was found to be more accurate for tumor regions, while the BC method performed better in certain organs and non-tumor areas. Comparisons between 30-minute and 10-minute [^{89}Zr]-atezolizumab scans for separation showed that the longer acquisition yielded lower bias and noise for both methods. However, due to the limited sample size, all statistical results should be interpreted with caution. Further studies with a larger patient cohort, different tracers, and improved separation algorithms are needed to advance clinical applications of dual-tracer PET imaging.

5. Ethical Statement

The masks used do not contain any patient specific information on the Habrók cluster and a UMCG computer was used to generate the patient masks. Patients have provided a consent form for reuse of their data in other studies. Responsible use of AI has been followed according to the 10 RUG guidelines during the course of this project. ChatGTP was used for flow and grammatical feedback and correction for this report. The supplementary materials used the help of GenAI for writing code based on pseudocode, locating errors, and generating comments.

6. References

https://doi.org/10.1021/acs.chemrev.9b00738

Alberts, I., Schepers, R., Zeimpekis, K., Sari, H., Rominger, A., & Afshar-Oromieh, A. (2023). Combined [68 Ga]Ga-PSMA-11 and low-dose 2-[18F]FDG PET/CT using a long-axial field of view scanner for patients referred for [177Lu]-PSMA-radioligand therapy. *European Journal of Nuclear Medicine and Molecular Imaging*, *50*(3), 951–956. https://doi.org/10.1007/s00259-022-05961-z

Alfuraih, A. A., Alzimami, K., & Ma, A. K. (2021). Investigation of 18F and 89Zr Isotopes Self-Absorption and Dose Rate Parameters for PET Imaging. *Dose-Response*, *19*(3), 15593258211028467. https://doi.org/10.1177/15593258211028467

Ashraf, M. A., & Goyal, A. (2025). Fludeoxyglucose (18F). In *StatPearls*. StatPearls Publishing. http://www.ncbi.nlm.nih.gov/books/NBK557653/

Bensch, F., van der Veen, E. L., Lub-de Hooge, M. N., Jorritsma-Smit, A., Boellaard, R., Kok, I. C., Oosting, S. F., Schröder, C. P., Hiltermann, T. J. N., van der Wekken, A. J., Groen, H. J. M., Kwee, T. C., Elias, S. G., Gietema, J. A., Bohorquez, S. S., de Crespigny, A., Williams, S.-P., Mancao, C., Brouwers, A. H., … de Vries, E. G. E. (2018). 89Zr-atezolizumab imaging as a non-invasive approach to assess clinical response to PD-L1 blockade in cancer. *Nature Medicine*, *24*(12), 1852–1858. https://doi.org/10.1038/s41591-018-0255-8

Bland, J. M., & Altman, D. G. (1999). Measuring agreement in method comparison studies. *Statistical Methods in Medical Research*, *8*(2), 135–160. https://doi.org/10.1177/096228029900800204

Boellaard, R., Delgado-Bolton, R., Oyen, W. J. G., Giammarile, F., Tatsch, K., Eschner, W., Verzijlbergen, F. J., Barrington, S. F., Pike, L. C., Weber, W. A., Stroobants, S., Delbeke, D., Donohoe, K. J., Holbrook, S., Graham, M. M., Testanera, G., Hoekstra, O. S., Zijlstra,

J., Visser, E., … European Association of Nuclear Medicine (EANM). (2015). FDG PET/CT: EANM procedure guidelines for tumour imaging: version 2.0. *European Journal of Nuclear Medicine and Molecular Imaging*, *42*(2), 328–354. https://doi.org/10.1007/s00259-014-2961-x

Calderón, E., Kiefer, L. S., Schmidt, F. P., Lan, W., Brendlin, A. S., Reinert, C. P., Singer, S., Reischl, G., Hinterleitner, M., Dittmann, H., la Fougère, C., & Trautwein, N. F. (2025). One-day dual-tracer examination in neuroendocrine neoplasms: A real advantage of low activity LAFOV PET imaging. *European Journal of Nuclear Medicine and Molecular Imaging*, *52*(7), 2463–2476. https://doi.org/10.1007/s00259-025-07073-w

Chiu, K. W. H., Chiang, C. L., Chan, K. S. K., Hui, Y., Ren, J., Wei, X., Ng, K. S., Lee, H. F. V., Chia, N. H., Cheung, T.-T., Chan, S., Chan, A. C.-Y., Ng, K. C. K., Seto, W. K. W., Khong, P.-L., & Kong, F.-M. (2024). Dual-tracer PET/CT in the management of hepatocellular carcinoma. *JHEP Reports*, *6*(7), 101099. https://doi.org/10.1016/j.jhepr.2024.101099

Cui, J., Gong, K., Guo, N., Wu, C., Meng, X., Kim, K., Zheng, K., Wu, Z., Fu, L., Xu, B., Zhu, Z., Tian, J., Liu, H., & Li, Q. (2019). PET image denoising using unsupervised deep learning. *European Journal of Nuclear Medicine and Molecular Imaging*, *46*(13), 2780–2789. https://doi.org/10.1007/s00259-019-04468-4

Defrise, M., Kinahan, P. E., & Michel, C. J. (2005). Image Reconstruction Algorithms in PET. In D. L. Bailey, D. W. Townsend, P. E. Valk, & M. N. Maisey (Eds.), *Positron Emission Tomography: Basic Sciences* (pp. 63–91). Springer. https://doi.org/10.1007/1-84628-007-9_4

Ding, W., Yu, J., Zheng, C., Fu, P., Huang, Q., Feng, D. D., Yang, Z., Wahl, R. L., & Zhou, Y. (2022). Machine Learning-Based Noninvasive Quantification of Single-Imaging Session Dual-Tracer 18F-FDG and 68Ga-DOTATATE Dynamic PET-CT in Oncology. *IEEE Transactions on Medical Imaging*, *41*(2), 347–359. https://doi.org/10.1109/TMI.2021.3112783

Greve, D. N., Svarer, C., Fisher, P. M., Feng, L., Hansen, A. E., Baare, W., Rosen, B., Fischl, B., & Knudsen, G. M. (2014). Cortical Surface-based Analysis Reduces Bias and Variance in Kinetic Modeling of Brain PET Data. *NeuroImage*, *92*, 225–236. https://doi.org/10.1016/j.neuroimage.2013.12.021

Joshi, A. D., Fessler, J. A., & Koeppe, R. A. (2008). Signal separation and parameter estimation in non-invasive dual-tracer PET. *NeuroImage*, *41*, T25. https://doi.org/10.1016/j.neuroimage.2008.04.199

Kadrmas, D. J., & Hoffman, J. M. (2013). Methodology for Quantitative Rapid Multi-Tracer PET Tumor Characterizations. *Theranostics*, *3*(10), 757–773. https://doi.org/10.7150/thno.5201

Kadrmas, D. J., Rust, T. C., & Hoffman, J. M. (2013). Single-scan dual-tracer FLT+FDG PET tumor characterization. *Physics in Medicine and Biology*, *58*(3), 429–449. https://doi.org/10.1088/0031-9155/58/3/429

Lin, Y., Gao, H., Zheng, J., Al-Ibraheem, A., Hu, P., & Shi, H. (2024). Clinical Explorations of [68Ga] Ga-FAPI-04 and [18F] FDG Dual-Tracer Total-body PET/CT and PET/MR Imaging. *Seminars in Nuclear Medicine*, *54*(6), 904–913. https://doi.org/10.1053/j.semnuclmed.2024.09.009

Linders, D. G. J., Deken, M. M., van Dam, M. A., Wasser, M. N. J. M., Voormolen, E. M. C., Kroep, J. R., van Dongen, G. a. M. S., Vugts, D., Oosterkamp, H. M., Straver, M. E., van de Velde, C. J. H., Cohen, D., Dibbets-Schneider, P., van Velden, F. H. P., Pereira Arias-Bouda, L. M., Vahrmeijer, A. L., Liefers, G. J., de Geus-Oei, L. F., & Hilling, D. E. (2023). 89Zr-Trastuzumab PET/CT Imaging of HER2-Positive Breast Cancer for Predicting Pathological Complete Response after Neoadjuvant Systemic Therapy: A Feasibility Study. *Cancers*, *15*(20), 4980. https://doi.org/10.3390/cancers15204980

Liu, G., Mao, W., Yu, H., Hu, Y., Gu, J., & Shi, H. (2023). One-stop [18F]FDG and [68Ga]Ga-DOTA-FAPI-04 total-body PET/CT examination with dual-low activity: A

feasibility study. *European Journal of Nuclear Medicine and Molecular Imaging*, *50*(8), 2271–2281. https://doi.org/10.1007/s00259-023-06207-2

Pan, B., Marsden, P. K., & Reader, A. J. (2025). Self-supervised parametric map estimation for multiplexed PET with a deep image prior. *Physics in Medicine & Biology*, *70*(4), 045002. https://doi.org/10.1088/1361-6560/ada717

Tai, Y., & Piccini, P. (2004). Applications of positron emission tomography (PET) in neurology. *Journal of Neurology, Neurosurgery, and Psychiatry*, *75*(5), 669–676. https://doi.org/10.1136/jnnp.2003.028175

TotalSegmentator: Robust Segmentation of 104 Anatomic Structures in CT Images | Radiology: Artificial Intelligence. (n.d.). Retrieved June 24, 2025, from https://pubs.rsna.org/doi/10.1148/ryai.230024

Trotter, J., Pantel, A. R., Teo, B.-K. K., Escorcia, F. E., Li, T., Pryma, D. A., & Taunk, N. K. (2023). Positron Emission Tomography (PET)/Computed Tomography (CT) Imaging in Radiation Therapy Treatment Planning: A Review of PET Imaging Tracers and Methods to Incorporate PET/CT. *Advances in Radiation Oncology*, *8*(5), 101212. https://doi.org/10.1016/j.adro.2023.101212

Tsoumpas, C., & Thielemans, K. (2009). Direct parametric reconstruction from dynamic projection data in emission tomography including prior estimation of the blood volume component. *Nuclear Medicine Communications*, *30*(7), 490–493. https://doi.org/10.1097/mnm.0b013e32832cc1d7

Vraka, C., Murgaš, M., Rischka, L., Geist, B. K., Lanzenberger, R., Gryglewski, G., Zenz, T., Wadsak, W., Mitterhauser, M., Hacker, M., Philippe, C., & Pichler, V. (2022). Simultaneous radiomethylation of [11C]harmine and [11C]DASB and kinetic modeling approach for serotonergic brain imaging in the same individual. *Scientific Reports*, *12*, 3283. https://doi.org/10.1038/s41598-022-06906-0

Wei, W., Rosenkrans, Z. T., Liu, J., Huang, G., Luo, Q.-Y., & Cai, W. (2020). ImmunoPET:

Concept, Design, and Applications. *Chemical Reviews*, *120*(8), 3787–3851. https://doi.org/10.1021/acs.chemrev.9b00738

7. Appendix

7.1. Separation with 30 minute [^{89}Zr]-atezolizumab Acquisition

Table 7.1.1. BA Plot values for 30 minute [^{89}Zr]-atezolizumab Acquisition

Tumor Label	Ref Intensity	BC Intensity	EM Intensity	% Difference BC	% Difference EM
Tumor Sacrum 1	1.8955	1.8683	1.8674	1.4468	1.4961
Tumor Sacrum 2	1.8365	1.8342	1.8122	0.12765	1.3337
Tumor Sacrum 3	1.7014	1.6774	1.6471	1.4221	3.2466
Tumor Sacrum 4	1.8392	1.7991	1.7878	2.2028	2.8328
Tumor Liver 1	17.174	16.950	17.229	1.3119	-0.31821
Tumor Liver 2	17.116	16.681	17.168	2.5730	-0.30092
Tumor Liver 3	16.122	15.838	16.197	1.7736	-0.46359
Tumor Liver 4	16.751	16.305	16.777	2.7016	-0.15420
Tumor Spleen 1	28.388	26.494	28.333	6.9028	0.19423
Tumor Spleen 2	29.052	27.447	28.854	5.6820	0.68116
Tumor Spleen 3	27.682	25.638	27.711	7.6652	-0.10532
Tumor Spleen 4	27.816	25.563	27.667	8.4404	0.53847
Liver	2.7498	2.7221	2.7508	1.0113	-0.03826
Spleen	0.52999	0.48994	0.43680	7.8534	19.279
Sacrum	0.99752	0.97139	0.99459	2.6542	0.29436

Table 7.1.2. SD vs. bias for 30 minute [^{89}Zr]-atezolizumab Acquisition ROI-level

Liver							
Method	Region	Bias	SD	NRMSE	RefIntensity	ReconIntensity	Absolute Difference
EM	Tumors	0.30833	0.46106	0.55466	16.7908	16.8425	-0.051771
EM	Selected Organs	0.038272	0.081115	0.089690	2.7498	2.7508	-0.001052
BC	Tumors	2.0675	0.31446	2.0913	16.7908	16.4436	0.347144
BC	Selected Organs	1.0063	0.045560	1.0073	2.7498	2.7221	0.027670
Sacrum							
Method	Region	Bias	SD	NRMSE	RefIntensity	ReconIntensity	Absolute Difference

EM	Tumors	2.1996	3.3969	4.0468	1.8172	1.7772	0.0399713
EM	Selected Organs	0.29392	0.18881	0.34934	0.99752	0.99459	0.0029319
BC	Tumors	1.3127	2.0393	2.4252	1.8172	1.7933	0.023854
BC	Selected Organs	2.6194	0.12806	2.6226	0.99752	0.97139	0.026129
Spleen							
Method	Region	Bias	SD	NRMSE	RefIntensity	ReconIntensity	Absolute Difference
EM	Tumors	0.32983	0.57269	0.66088	28.234	28.141	0.093126
EM	Spleen	17.584	0.72373	17.599	0.52999	0.43680	0.093192

Table 7.1.3. SD vs. bias and NRMSE for 30 minute [^{89}Zr]-atezolizumab Acquisition Voxel-level

Method	Region	Bias	SD	NRMSE	RefIntensity	ReconIntensity
EM	Tumors	1.2301	5.0274	5.1757	15.476	15.449
EM	Selected Organs	3.8760	10.940	11.606	2.2300	2.2158
EM	Tumors	10.765	2.7257433	11.105	1.3679	1.3544
BC	Selected Organs	3.6102	7.8431754	9.5708	15.476	14.710

7.2. Separation with 10 minute [^{89}Zr]-atezolizumab Acquisition

Table 7.2.1. BA Plot values for 10 minute [^{89}Zr]-atezolizumab Acquisition ROI-level

Tumor Label	Ref Intensity	BC Intensity	EM Intensity	% Difference BC	% Difference EM
Tumor Sacrum 1	1.8955	1.9299	1.9591	-1.7954	-3.2998
Tumor Sacrum 2	1.8365	1.9011	1.8909	-3.4561	-2.9171
Tumor Sacrum 3	1.7014	1.7038	1.6993	-0.13748	0.12174
Tumor Sacrum 4	1.8392	1.8335	1.8293	0.30911	0.54162
Tumor Liver 1	17.174	16.902	17.188	1.5957	-0.08377
Tumor Liver 2	17.116	16.850	17.318	1.5666	-1.1712
Tumor Liver 3	16.122	15.916	16.279	1.2825	-0.97137
Tumor Liver 4	16.751	16.370	16.834	2.3013	-0.49398
Tumor Spleen 1	28.388	26.586	28.381	6.5583	0.02420
Tumor Spleen 2	29.052	27.388	28.795	5.8965	0.88806
Tumor Spleen 3	27.682	25.687	27.778	7.4747	-0.34725
Tumor Spleen 4	27.816	25.690	27.798	7.9487	0.0655

Liver	2.7498	2.7235	2.7529	0.95961	-0.11605
Spleen	0.52999	0.49267	0.44291	7.2979	17.900
Sacrum	0.99752	0.97667	1.0024	2.1124	-0.48307

Table 7.2.2. SD vs. bias for 10 minute [^{89}Zr]-atezolizumab Acquisition

Liver							
Method	Region	Bias	SD	NRMSE	RefIntensity	ReconIntensity	Absolute Difference
EM	Tumors	0.67948	0.46106	0.82114	16.791	16.905	-0.11409
EM	Selected Organs	0.11612	0.08111	0.14164	2.7498	2.7529	-0.0031929
BC	Tumors	1.6742	0.73033	1.8266	16.791	16.510	0.28112
BC	Selected Organs	0.95502	0.03615	0.95570	2.7498	2.72349	0.02626
Sacrum							
Method	Region	Bias	SD	NRMSE	RefIntensity	ReconIntensity	Absolute Difference
EM	Tumors	1.4089	3.3969	3.6774	1.8172	1.8428	-0.025602
EM	Selected Organs	0.48424	0.18881	0.51975	0.99752	1.0024	-0.0048304
BC	Tumors	1.2615	1.9992	2.3640	1.8172	1.8401	-0.022924
BC	Selected Organs	2.0903	0.28212	2.1093	0.99752	0.97667	0.020851
Spleen							
Method	Region	Bias	SD	NRMSE	RefIntensity	ReconIntensity	Absolute Difference
EM	Tumors	0.16437	0.57269	0.59582	28.234	28.188	0.04641
EM	Selected Organs	16.430	0.72373	16.446	0.52999	0.44291	0.08708
BC	Tumors	6.7185	0.95134	6.7855	28.234	26.338	1.8969
BC	Selected Organs	7.0409	0.64884	7.0708	0.52999	0.49267	0.03732

Table 7.2.3. SD vs. bias and NRMSE for 10 minute [^{89}Zr]-atezolizumab Acquisition Voxel-level

Method	Region	Bias	SD	NRMSE	RefIntensity	ReconIntensity
EM	Tumors	0.20056	0.37214	0.42274	15.476	15.507
EM	Selected Organs	0.48661	0.082430	0.49354	2.2300	2.2191
EM	Tumors	4.5939	0.63052	4.6370	15.476	14.765
BC	Selected Organs	1.2320	0.043515	1.2328	2.2300	2.2025

7.3. Separation with 30 minute vs. 10 minute [^{89}Zr]-atezolizumab Acquisition

Table 7.3.1. Summary ANOVA Table 30 minute vs. 10 minute [^{89}Zr]-atezolizumab Acquisition for tumors

SUMMARY	*Count*	*Sum*	*Average*	*Variance*
Tumor Spleen 1	2	-0.348576	-0.174288	5.255872061
Tumor Spleen 2	2	-3.328498	-1.664249	6.421796885
Tumor Spleen 3	2	1.284592	0.642296	1.216098101
Tumor Spleen 4	2	2.511887	1.2559435	1.792975991
Tumor Sacrum 1	2	2.907615	1.4538075	0.04026980101
Tumor Sacrum 2	2	4.139581	2.0697905	0.506465769
Tumor Sacrum 3	2	3.056134	1.528067	0.120578801
Tumor Sacrum 4	2	5.002902	2.501451	0.08014166266
Tumor Liver 1	2	13.46108	6.73054	0.05935459488
Tumor Liver 2	2	11.578504	5.789252	0.02300298005
Tumor Liver 3	2	15.139889	7.5699445	0.01814836364
Tumor Liver 4	2	16.389052	8.194526	0.1208991965
10min	12	29.544296	2.462024667	13.75607865
30min	12	42.249866	3.520822167	8.08593491

ANOVA

Source of Variation	*SS*	*df*	*MS*	*F*	*P-value*	*F crit*
Tumors	231.3328578	11	21.0302598	25.9071912	0.00000285137043	2.81793047
10 min v 30 min	6.726312876	1	6.726312876	8.286149359	0.01500970745	4.844335675
Error	8.929291331	11	0.8117537573			
Total	246.988462	23				